

# Binary Neutron Star Mergers: Dependence on the Nuclear Equation of State

Kenta Hotokezaka,<sup>1</sup> Koutarou Kyutoku,<sup>2</sup> Hirotada Okawa,<sup>2</sup> Masaru Shibata,<sup>2</sup> and Kenta Kiuchi<sup>2</sup>

<sup>1</sup>*Department of Physics, Kyoto University, Kyoto 606-8502, Japan*

<sup>2</sup>*Yukawa Institute for Theoretical Physics, Kyoto University, Kyoto 606-8502, Japan*

We perform a numerical-relativity simulation for the merger of binary neutron stars with 6 nuclear-theory-based equations of state (EOSs) described by piecewise polytropes. Our purpose is to explore the dependence of the dynamical behavior of the binary neutron star merger and resulting gravitational waveforms on the EOS of the supernuclear-density matter. The numerical results show that the merger process and the first outcome are classified into three types; (i) a black hole is promptly formed, (ii) a short-lived hypermassive neutron star (HMNS) is formed, (iii) a long-lived HMNS is formed. The type of the merger depends strongly on the EOS and on the total mass of the binaries. For the EOS with which the maximum mass is larger than  $2M_{\odot}$ , the lifetime of the HMNS is longer than 10 ms for a total mass  $m_0 = 2.7M_{\odot}$ . A recent radio observation suggests that the maximum mass of spherical neutron stars is  $M_{\max} \geq 1.97 \pm 0.04M_{\odot}$  in one  $\sigma$  level. This fact and our results support the possible existence of a HMNS soon after the onset of the merger for a typical binary neutron star with  $m_0 = 2.7M_{\odot}$ . We also show that the torus mass surrounding the remnant black hole is correlated with the type of the merger process; the torus mass could be large,  $\geq 0.1M_{\odot}$ , in the case that a long-lived HMNS is formed. We also show that gravitational waves carry information of the merger process, the remnant, and the torus mass surrounding a black hole.

PACS numbers: 04.25.dk, 04.30.DB, 97.60.JD

## I. INTRODUCTION

The coalescence of binary neutron stars is one of the most promising sources for kilometer-size laser-interferometric gravitational-wave detectors such as LIGO [1], VIRGO [2], and GEO600 [3]. A statistical study based on the stellar evolution synthesis (e.g., Ref. [4]) suggests that detection rate  $\sim 10 \text{ yr}^{-1}$  may be achieved by advanced detectors such as advanced LIGO [5], advanced VIRGO [6], and LCGT [7], which will be in operation in this decade. The merger of binary neutron stars will be a viable laboratory for studying supernuclear-density matter through gravitational-wave observations. For clarifying the nature as the sources of gravitational waves and for extracting their physical information, theoretical templates of gravitational waves are needed. Because the merger is a highly dynamical process and proceeds in strong gravitational fields, numerical relativity is the unique way for deriving the templates of gravitational waves.

The merger of binary neutron stars also has been proposed as a likely candidate for the central engine of short  $\gamma$ -ray bursts (GRBs) [8, 9]. The observations have shown that the central engine supplies a large amount of energy  $\gtrsim 10^{48}$  ergs in a short time scale  $\lesssim 2$  s [10]. According to a standard scenario based on the merger hypothesis, a stellar-mass black hole surrounded by a hot massive torus should be formed after the merger. Possible relevant processes to extract the energy of this black hole-torus system for launching a relativistic jet are neutrino-antineutrino pair annihilation and/or magnetically driven mechanisms. Recent numerical studies (e.g., Ref. [11]) suggest that if the torus has a mass  $\gtrsim 0.1M_{\odot}$ , it could supply the required energy of short GRBs by the neutrino mechanism. The amount of the mass of the

remnant torus depends on the dynamical behavior of the merger process of binary neutron stars. Thus, the issue is to clarify how the formation process of a massive torus depends on the dynamics of the merger, on the equation of state (EOS) of neutron stars, and on parameters of the binary such as total mass and mass ratio, for understanding the formation mechanism of the central engine of short GRBs.

The supernuclear-density EOS plays a key role for determining the merger process of binary neutron stars. For example, for a given mass, the outcome of the merger depends strongly on the EOS: For soft EOSs, the merger results in prompt formation of a black hole. On the other hand, for stiff EOSs, a hypermassive neutron star (HMNS) is formed [12–14]. However, the actual supernuclear-density EOS is still unknown because of our poor knowledge about the properties of the matter above the nuclear density.

In this paper, we extend the previous works for a long-term simulation of binary neutron stars (e.g., Refs. [15–17]) from the following motivation. Recently, a piecewise-polytropic EOS for the cold EOS, based on the nuclear theoretical calculations, was proposed by Read *et al.*, and by Özel and Psaltis [18, 19]. With only four parameters, the piecewise-polytropic EOS can approximate any candidate of the EOS of supernuclear-density matter. By using this EOS, we can systematically study the effects of the possible EOSs on phenomena related to the supernuclear-density matter, such as the merger of binary neutron stars.

In this work, we report our latest numerical-simulation results for the merger of equal-mass binary neutron stars, for which the total masses are in the range of  $2.7M_{\odot}$ – $3.0M_{\odot}$ . To systematically study the effects of the EOS on the merger, we use 6 different stiff EOSs which are de-

scribed in Ref. [18]. In the present simulation, we follow the inspiral motion for 5–7 orbits and the merger process up to formation of a stationary black hole or HMNS. After a black hole is formed, we study the dependence of the properties of the resulting torus, such as its mass, on the EOS and the total mass of the binaries. We also extract gravitational waves and show the dependence of the gravitational waveforms and their spectra on the EOS.

The paper is organized as follows. In Sec. II, we summarize the formulation and numerical schemes employed in our numerical code SACRA, and the EOS employed in this study. In Sec. III.A, we describe our simulation results for the typical cases of the merger. We define three types of the merger process, which clearly classify the dependence of the dynamical behavior of the merger on the EOSs. In Sec. III.B, we summarize the characteristic features of gravitational waveforms for each type. Section IV is devoted to a summary. Throughout this paper we use the geometrical units of  $c = G = 1$  where  $c$  and  $G$  are the speed of light and gravitational constant, respectively.

## II. FORMULATION

### A. Numerical method

We follow the late inspiral and merger phases of binary neutron stars using a numerical-relativity code, called SACRA, described in Ref. [20]. SACRA employs a moving-puncture version of the Baumgarte-Shapiro-Shibata-Nakamura formalism [21–23] to solve Einstein’s evolution equation without imposing any symmetry. In SACRA, we evolve a conformal factor  $W \equiv \gamma^{-1/6}$ , the conformal three metric  $\tilde{\gamma}_{ij} = \gamma^{-1/3}\gamma_{ij}$ , the trace of extrinsic curvature  $K$ , the conformal trace-free extrinsic curvature  $\tilde{A}_{ij} = \gamma^{-1/3}(K_{ij} - K\gamma_{ij}/3)$ , and an auxiliary variable  $\tilde{\Gamma}^i \equiv -\partial_j \tilde{\gamma}^{ij}$ . Here  $\gamma_{ij}$  is the three metric,  $K_{ij}$  is the extrinsic curvature, and  $\gamma \equiv \det(\gamma_{ij})$ . In the numerical simulation, a fourth-order finite differencing scheme in space and time is used implementing an adaptive mesh refinement (AMR) algorithm (at refinement boundaries, a second-order interpolation scheme is partly adopted). The advection terms such as  $\beta^i \partial_i \tilde{\gamma}_{jk}$  are evaluated by a fourth-order non-centered finite difference [24]. A fourth-order Runge-Kutta method is employed for the time evolution.

Following Ref. [24], we adopt a moving-puncture gauge condition as

$$(\partial_t - \beta^j \partial_j)\beta^j = 0.75B^j, \quad (1)$$

$$(\partial_t - \beta^j \partial_j)B^i = (\partial_t - \beta^j \partial_j)\tilde{\Gamma}^i - \eta_s B^i, \quad (2)$$

where  $B^i$  is an auxiliary variable and  $\eta_s$  is an arbitrary constant. In the present paper, we set  $\eta_s \simeq 3/M$ . Here,  $M$  denotes the mass for each neutron star in isolation.

For the hydrodynamics, we employ a high-resolution central scheme by Kurganov and Tadmor [25] with a

third-order piecewise parabolic interpolation and with a steep min-mod limiter.

In SACRA, an AMR algorithm is adopted (see Ref. [20] for details). In the present work, we prepare seven refinement levels both to accurately resolve the structure of two neutron stars and to extract gravitational waves in a local wave zone. In our simulations, two sets of four finer domains comoving with the neutron stars cover the region in their vicinity. The other three coarser domains cover both neutron stars by a wider domain with their origins being fixed approximately at the center of mass of the binary. Each refinement domain consists of the uniform, vertex-centered Cartesian grids with  $(2N + 1, 2N + 1, N + 1)$  grid points for  $(x, y, z)$  with the equatorial plane symmetry at  $z = 0$  imposed. The half of the edge length of the largest domain (i.e., the distance from the origin to outer boundaries along each axis) is denoted by  $L$  which is chosen to be  $\gtrsim \lambda_0$ , where  $\lambda_0 = \pi/\Omega_0$  is the initial wavelength of gravitational waves. The grid spacing for each domain is then  $h_l = L/(2^l N)$ , where  $l = 0-6$ . In this work, we typically choose  $N = 60$ . With this grid resolution, the semi-major diameter of each neutron star is covered by about 100 grid points (cf. Table II). In addition, we performed numerical simulations with lower grid resolutions,  $N = 36, 42$ , and 50, to check the convergence of the numerical results. The property of the convergence is essentially the same as in Refs. [20, 23].

### B. Models of Equation of State

The parameterized piecewise-polytropic EOS [18, 19] is useful to systematically study the dependence of the dynamical behavior of the merger on the EOS of the supernuclear-density matter. In this work, we employ a parameterized piecewise-polytropic EOS proposed by Read *et al.* [18]. This EOS is written in terms of four segments of polytropes

$$P = K_i \rho^{\Gamma_i} \quad (3)$$

( for  $\rho_i \leq \rho < \rho_{i+1}$ ,  $0 \leq i \leq 3$  ),

where  $\rho$  is the rest-mass density,  $P$  is the pressure,  $K_i$  is the polytropic constant, and  $\Gamma_i$  is the adiabatic index. We refer to the pressure in the form of Eq. (3) as the cold-part pressure,  $P_{\text{cold}}$ . At each boundary of the piecewise polytropes,  $\rho = \rho_i$ , the pressure is required to be continuous, i.e.,  $K_i \rho_i^{\Gamma_i} = K_{i+1} \rho_i^{\Gamma_{i+1}}$ . Read *et al.* determine these parameters in the following manner [18]. First, they fix the EOS of the crust as  $\Gamma_0 = 1.357$  and  $K_0 = 3.594 \times 10^{13}$  in the cgs unit. Then they determine  $\rho_2 = 1.85\rho_{\text{nucl}}$  and  $\rho_3 = 3.70\rho_{\text{nucl}}$  where  $\rho_{\text{nucl}} = 2.7 \times 10^{14}$  g/cm<sup>3</sup> is the nuclear saturation density. With this preparation, they choose the following four parameters as a set of free parameters:  $\{P_1, \Gamma_1, \Gamma_2, \Gamma_3\}$ . Here  $P_1$  is the pressure at  $\rho = \rho_2$ , and from this,  $K_1$  and  $K_i$  are determined by  $K_1 = P_1/\rho_2^{\Gamma_1}$  and  $K_{i+1} = K_i \rho_i^{\Gamma_i - \Gamma_{i+1}}$ . There-

TABLE I: Parameters of the piecewise-polytropic EOS, the maximum mass of spherical neutron stars,  $M_{\max}$ , and the radius of a spherical neutron star of mass  $M = 1.4M_{\odot}$ ,  $R_{1.4}$ , for each EOS. Composition means strongly interacting components (n=neutron, p=proton, H=hyperon, Q=quark,  $\pi^0$ =pion) and APR4, SLy, H3, H4, and ALF2 include leptonic components.

| EOS  | $\log P_1$ (dyne/cm <sup>2</sup> ) | $\Gamma_1$ | $\Gamma_2$ | $\Gamma_3$ | $M_{\max}(M_{\odot})$ | $R_{1.4}$ (km) | Approach                     | composition |
|------|------------------------------------|------------|------------|------------|-----------------------|----------------|------------------------------|-------------|
| APR4 | 34.269                             | 2.830      | 3.445      | 3.348      | 2.213                 | 11.428         | Variational-method           | np          |
| SLy  | 34.348                             | 3.005      | 2.988      | 2.851      | 2.049                 | 11.736         | Effective-one-body potential | np          |
| H3   | 34.646                             | 2.787      | 1.951      | 1.901      | 1.788                 | 13.840         | Relativistic mean field      | npH         |
| H4   | 34.669                             | 2.909      | 2.246      | 2.144      | 2.032                 | 13.759         | Relativistic mean field      | npH         |
| ALF2 | 34.055                             | 4.070      | 2.411      | 1.890      | 2.086                 | 13.188         | APR+Quark matter             | npQ         |
| PS   | 34.671                             | 2.216      | 1.640      | 2.365      | 1.755                 | 15.472         | Pion condensation            | n $\pi^0$   |

fore the EOS is specified by choosing the four parameters  $\{P_1, \Gamma_1, \Gamma_2, \Gamma_3\}$ .

In this paper, we adopt 6 models of piecewise-polytropic EOS which describe the following EOSs based on nuclear theoretical calculations.

1. APR4: derived by a variational-method with the AV18 2-body potential, the UIX 3-body potential, and relativistic boost corrections (see Ref. [26]);
2. SLy: derived by using an effective potential approach of the Skyrme type (see Ref. [27]);
3. H3: derived by a relativistic mean-field approach including hyperons. The incompressibility, the effective mass, and the nucleon-meson coupling are chosen to be  $K = 300$  MeV,  $m_*/m_n = 0.7$ , and  $x_{\sigma} = 0.6$ . Here  $m_n$  is the nucleon-mass (see Refs. [28, 29]);
4. H4: the same as H3 but for  $x_{\sigma} = 0.72$  (see Refs. [28, 29]);
5. ALF2: a hybrid EOS which describes nuclear matter for a low density and color-flavor-locked quark matter for a high density. The transition density and the interaction parameter are chosen to be  $\rho_c = 3\rho_{\text{nucl}}$  and  $c = 0.3$  (see Ref. [30]);
6. PS: derived by using a potential approach. This EOS describes a neutron matter with pion condensation (see Ref. [31]).

Table I lists the parameters of piecewise-polytropic EOSs employed in this work. These EOSs are relatively stiff, and hence, the maximum mass of spherical neutron stars is larger than  $1.75M_{\odot}$ . The choice of these EOSs is motivated by the recent discovery of a heavy neutron star with mass  $1.97 \pm 0.04M_{\odot}$  (one  $\sigma$  error) [32]. This value has become the new standard for the minimum value of the neutron star maximum mass [33, 34].

The thermal pressure should be taken into account for numerical simulations, because matter in the merged neutron stars becomes hot with temperature to  $T \geq 10$  MeV due to the shock heating at the merger (e.g., Refs. [35, 36]). In this case, the thermal energy is not

negligible. To approximately include the thermal pressure, we employ the EOS which is described by

$$P(\rho, \varepsilon) = P_{\text{cold}}(\rho) + P_{\text{th}}(\rho, \varepsilon), \quad (4)$$

where  $\varepsilon$  is the specific internal energy,  $P_{\text{cold}}$  is the pressure determined by the piecewise-polytropic EOS, and  $P_{\text{th}}$  is the thermal part of the pressure which is given by

$$P_{\text{th}} = (\Gamma_{\text{th}} - 1)(\varepsilon - \varepsilon_{\text{cold}})\rho. \quad (5)$$

Here  $\varepsilon_{\text{cold}}$  is determined from  $P_{\text{cold}}$  by the first law of thermodynamics [18]. In our simulations, we focus only on the case that the shock heating efficiency is relatively low, i.e.,  $\Gamma_{\text{th}} = 1.357$ . To study the effect of thermal pressure on the outcome of the merger, we also employed  $\Gamma_{\text{th}} = 1.5, 1.7$ , and  $1.8$  for a few simulations with lower grid resolutions. We found that the outcome formed soon after the merger (a black hole or HMNS) depends very weakly on the value of  $\Gamma_{\text{th}}$  (see also Ref. [13]), although the long-term evolution process of a HMNS depends on it [35].

### C. Initial data

We prepare binary neutron stars in quasiequilibrium states for the initial condition of numerical simulations. To track more than 5 quasicircular orbits with small eccentricity for deriving accurate gravitational waveforms in the late inspiral and merger phases, orbital separation of the initial configuration is chosen to be large enough that the time scale of gravitational radiation reaction is much longer than the orbital period of the binary.

The formulation and methods for a solution of Einstein's constraint equation and equations of hydrostatics are the same as those adopted in our previous works [16, 20, 44], except for the choice of EOSs. We assume the conformal flatness of the three metric  $\gamma_{ij} = \psi^4 f_{ij}$ , the maximal slicing condition  $K = 0$ , and their preservation in time. Here,  $\psi$  is a conformal factor and  $f_{ij}$  is the flat spatial metric. The piecewise-polytropic EOS described in the previous subsection is adopted to model the neutron star matter because the fluid inside the neutron stars in the late inspiral phase are believed to

TABLE II: Key parameters for the initial models adopted in the numerical simulation.  $m_0$  is the sum of the ADM masses of two neutron stars in isolation ( $2M$ );  $M_0^{\text{ADM}}$  and  $J_0^{\text{ADM}}$  are the ADM mass and angular momentum of the system, respectively;  $M_*$  is the baryon rest mass;  $\Omega_0$  is the angular velocity. We also show the setup of the grid structure for the computation with our AMR algorithm.  $\Delta x = h_6 = L/(2^6 N)$  is the grid spacing at the finest resolution domain with  $L$  being the location of the outer boundaries for each axis.  $R_{\text{diam}}$  denotes the number of the grid points assigned inside the semimajor diameter of the neutron stars.  $\lambda_0$  is the wavelength of gravitational waves of the initial configuration. In the last two columns, we show the simulation results for the rest mass of the torus  $M_{\text{torus}}$  and the type of the merger process for each model. The rest mass of the torus surrounding the black hole is determined at 1 ms after the black hole formation. For APR4-27, a HMNS with the lifetime  $\gg 10$  ms is formed. For H4-30, the type of the merger process is ambiguous because a black hole is formed at only 1.5 ms after the onset of the merger.

| Model   | $m_0$ | $M_0^{\text{ADM}}$ | $J_0^{\text{ADM}}$ | $M_*$ | $m_0\Omega_0$ | $\Delta x/m_0$ | $R_{\text{diam}}/\Delta x$ | $L/\lambda_0$ | $M_{\text{torus}}/M_\odot$ | type    |
|---------|-------|--------------------|--------------------|-------|---------------|----------------|----------------------------|---------------|----------------------------|---------|
| APR4-27 | 2.7   | 2.67               | 7.16               | 3.00  | 0.0221        | 0.043          | 99                         | 1.16          | -                          | III     |
| APR4-28 | 2.8   | 2.77               | 7.70               | 3.12  | 0.0221        | 0.041          | 102                        | 1.11          | 0.003                      | I       |
| APR4-29 | 2.9   | 2.87               | 8.26               | 3.26  | 0.0221        | 0.039          | 102                        | 1.05          | <0.001                     | I       |
| SLy-27  | 2.7   | 2.67               | 7.16               | 2.98  | 0.0221        | 0.045          | 101                        | 1.21          | 0.02                       | II      |
| SLy-28  | 2.8   | 2.77               | 7.70               | 3.12  | 0.0221        | 0.043          | 102                        | 1.15          | <0.001                     | I       |
| H3-27   | 2.7   | 2.68               | 7.39               | 2.94  | 0.0221        | 0.056          | 102                        | 1.50          | 0.05                       | II      |
| H3-29   | 2.9   | 2.87               | 8.27               | 3.18  | 0.0221        | 0.050          | 103                        | 1.34          | 0.01                       | I       |
| H4-27   | 2.7   | 2.68               | 7.39               | 2.94  | 0.0221        | 0.056          | 103                        | 1.50          | 0.18                       | III     |
| H4-29   | 2.9   | 2.87               | 8.27               | 3.18  | 0.0221        | 0.051          | 101                        | 1.37          | 0.02                       | II      |
| H4-30   | 3.0   | 2.97               | 8.85               | 3.30  | 0.025         | 0.048          | 102                        | 1.49          | 0.01                       | I or II |
| ALF2-27 | 2.7   | 2.67               | 7.17               | 2.98  | 0.0221        | 0.049          | 102                        | 1.32          | 0.16                       | III     |
| ALF2-29 | 2.9   | 2.87               | 8.51               | 3.22  | 0.0221        | 0.045          | 102                        | 1.22          | 0.02                       | II      |
| ALF2-30 | 3.0   | 2.97               | 8.85               | 3.34  | 0.0221        | 0.043          | 102                        | 1.32          | 0.003                      | I       |
| PS-27   | 2.7   | 2.68               | 7.57               | 2.88  | 0.020         | 0.073          | 92                         | 1.60          | 0.04                       | III     |
| PS-29   | 2.9   | 2.88               | 8.73               | 3.12  | 0.020         | 0.065          | 92                         | 1.48          | 0.02                       | II      |
| PS-30   | 3.0   | 2.97               | 8.85               | 3.24  | 0.025         | 0.056          | 102                        | 1.71          | 0.01                       | I       |

be well approximated by a cold, zero-temperature matter. The neutron stars are assumed to have an irrotational velocity field, which is believed to be an astrophysically realistic configuration [39, 40]. Numerical computations are performed using the spectral-method library, LORENE [41]. The details of the numerical methods and the analysis of quasiequilibrium states are summarized in Ref. [37] (see also Ref. [38]). We note that the virial error of the quasiequilibrium, which we define as the relative difference between the ADM and Komar masses, is always smaller than  $10^{-4}$  for our numerical solutions.

#### D. Gravitational wave extraction and waveforms

Gravitational waves are extracted by calculating the complex Weyl scalar  $\Psi_4$ , using the same procedure as in Ref. [20]. Gravitational waveforms are calculated by

$$h_+(t) - ih_\times(t) = - \lim_{r \rightarrow \infty} \int^t dt' \int^{t'} dt'' \Psi_4(t'', r). \quad (6)$$

Here we omit arguments  $\theta$  and  $\phi$ . We evaluate  $\Psi_4$  at a finite coordinate radius  $r = 400M_\odot \simeq 590$  km. In the standard spherical coordinate  $(r, \theta, \phi)$ ,  $\Psi_4$  can be expanded in the form

$$\Psi_4(t, r, \theta, \phi) = \sum_{lm} \Psi_4^{lm}(t, r) {}_{-2}Y_{lm}(\theta, \phi), \quad (7)$$

where  ${}_{-2}Y_{lm}$  are spin-weighted spherical harmonics of weight  $-2$  and  $\Psi_4^{lm}$  are expansion coefficients defined by this equation. In this work, we focus only on the  $(l, |m|) = (2, 2)$  mode.

We evaluate the amplitude of the Fourier spectrum of gravitational waves,

$$\tilde{h}(f) = \sqrt{\frac{|\tilde{h}_+(f)|^2 + |\tilde{h}_\times(f)|^2}{2}}, \quad (8)$$

where  $f$  is the frequency, and  $\tilde{h}_+(f)$  and  $\tilde{h}_\times(f)$  are the Fourier transformation of the plus and cross modes of gravitational waves observed along the  $z$  axis. The effective amplitude of gravitational waves for a given frequency is defined by,

$$h_{\text{eff}}(f) = f\tilde{h}(f). \quad (9)$$

Note that this is the most optimistic value for the effective amplitude. Actually, the amplitude of gravitational waves depends on an angle locating the source in the sky and on an angle specifying the orientation of orbital plane of the binary neutron star. The angular average of the effective amplitude is approximately  $\simeq 0.4h_{\text{eff}}$ .

#### E. Mass, linear momenta and angular momenta

We monitor the ADM mass  $M_{\text{ADM}}$ , the linear momentum  $P_i$ , and the angular momenta  $J_i$  during the evolu-

tion. These parameters are defined by the integrals on two surfaces of a coordinate radius  $r = 400, 300,$  and  $240M_\odot$ ,

$$M_{\text{ADM}}(r) = \frac{1}{16\pi} \int_r \sqrt{\gamma} \gamma^{ij} \gamma^{kl} (\gamma_{ik,j} - \gamma_{ij,k}) dS_l, \quad (10)$$

$$P_i(r) = \frac{1}{8\pi} \int_r \sqrt{\gamma} (K_i^j - K \gamma_i^j) dS_j, \quad (11)$$

$$J_i(r) = \frac{1}{8\pi} \epsilon_{ikl} \int_r \sqrt{\gamma} x^l (K^{jk} - K \gamma^{jk}) dS_j, \quad (12)$$

where  $dS_l$  is the surface element and  $\epsilon_{ijk}$  is the Levi-Civita symbol. Then, we extrapolate these quantities for  $r \rightarrow \infty$  to obtain the asymptotic value.

We also monitor the total baryon rest mass

$$M_* = \int \rho u^t \sqrt{-g} d^3x, \quad (13)$$

where  $u^t$  is the time-component of the four velocity, and  $g$  is the determinant of the space-time metric. After the black hole formation, we calculate the torus mass defined by

$$M_{\text{torus}} = \int_{r > r_{\text{AH}}} \rho u^t \sqrt{-g} d^3x, \quad (14)$$

where  $r_{\text{AH}}$  is the coordinate radius of the apparent horizon.

### III. NUMERICAL RESULTS

Table II lists the numerical models adopted in this paper. The simulations were performed from 5 – 7 orbits before the onset of the merger to 3 ms after the formation of a black hole or to the phase in which a HMNS relaxes to a quasi-stationary state.

#### A. Dynamics

The merger dynamics are determined primarily by three forces: gravity, pressure, and centrifugal forces. If its gravity is stronger than the other forces, the merged neutron star collapses to a black hole soon after the onset of the merger. On the other hand, if the other forces could overcome the gravity in a compact state, the core of the merged neutron star bounces and a rapidly rotating and oscillating HMNS is formed. This dynamical behavior depends on the EOS and on the total mass of the binary neutron star,  $m_0$ . In the following, we show the results of our numerical simulations focusing on the dynamical behavior of the merger.

##### 1. Classification of the merger process

It is natural to expect that a black hole is eventually formed after a merger of any binary neutron star,

because a typical total mass of binary neutron stars is  $\sim 2.7M_\odot$  [42], which is likely to exceed the maximum mass of spherical neutron stars. Although binary neutron stars have such a large total mass, a HMNS is often formed as a transient outcome of the merger, which is supported by the strong centrifugal force caused by rapid and differential rotation as well as by thermal pressure. Thus, one can classify the merger process and the resulting remnant of binary neutron stars into three types (see Table II):

- type I: A black hole is promptly formed;
- type II: A short-lived HMNS is formed ( $\tau_H < 5$  ms);
- type III: A long-lived HMNS is formed ( $\tau_H > 5$  ms).

Here  $\tau_H$  is a lifetime of a HMNS. We note that a massive and stable rigidly rotating neutron star may be formed if the total mass is only slightly larger than the maximum mass of spherical neutron stars or the contribution of the thermal pressure is significant. However, we do not consider this fourth possibility in this paper (but see Ref. [36]).

Figure 1 shows the snapshots of the density colormap for three types of the merger process. Since the dynamics of the binary neutron stars in the inspiral phase is similar among three types, we focus only on the dynamics after the onset of the merger in the following.

*Top panels; APR4-29 (type I).* Soon after the onset of the merger (Fig. 1, *top left*), the merged object collapses promptly to a black hole and tiny materials remain outside the black hole (Fig. 1, *top center*). The black filled circle denotes the inner region of the apparent horizon. Note that the spiral arms are formed and the materials in their outer region obtain angular momentum from the materials in the inner region by gravitational torques resulting from the non-axisymmetric structure. At  $\simeq 5$  ms after the onset of the merger, a quasi-stationary torus is formed with the maximum density  $\rho_{\text{max}} \sim 10^{11.5}$  g/cm<sup>3</sup>, and spreads to about 10 km from its center (Fig. 1, *top right*). However the torus mass is small  $\lesssim 10^{-3}M_\odot$ .

*Middle panels; H3-27 (type II).* After the onset of the merger, the merged core bounces due to strong centrifugal and pressure forces. The resulting HMNS has a double-core structure in which they rotate around each other (Fig. 1, *middle center*). At  $\simeq 5$  ms after the onset of the merger, the HMNS collapses to a black hole (Fig. 1 *middle right*), because its angular momentum decreases due to the emission of gravitational waves. We find that the collapse of the HMNS occurs during the phase in which the HMNS has a non-axisymmetric shape. The resulting torus around the black hole (Fig. 1 *middle right*) spreads to about 20 km. This torus has the maximum density  $\rho_{\text{max}} \sim 10^{12.5}$  g/cm<sup>3</sup>. In this case, the torus mass is  $\simeq 0.05M_\odot$ . The resulting black hole-torus system is a candidate for the central engine of short GRBs.

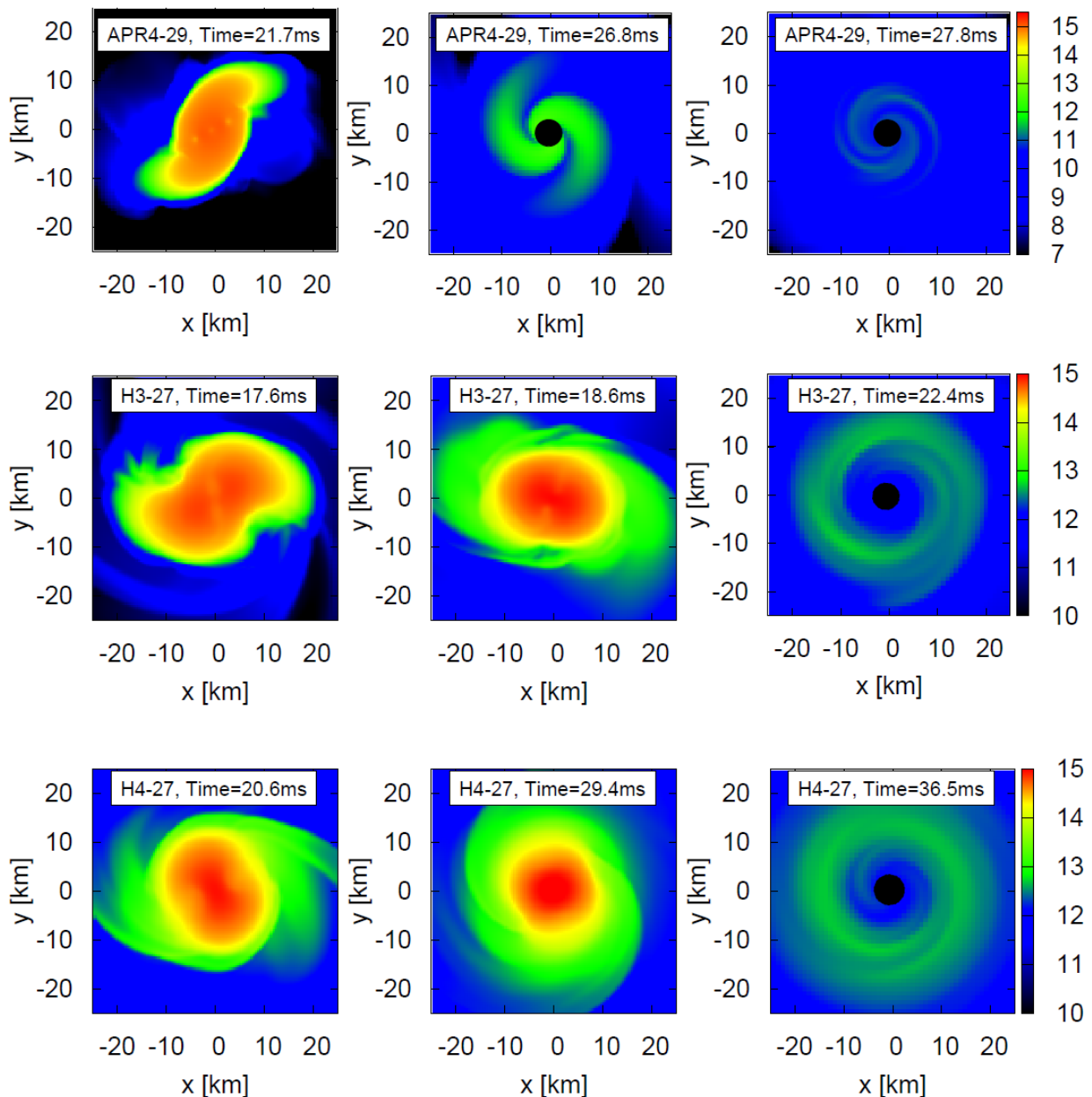


FIG. 1: Colormap of the density,  $\log \rho$  ( $\text{g}/\text{cm}^3$ ). *Top*, *middle*, and *bottom* rows show the snapshots for APR4-29, H3-27, and H4-27, respectively. The black filled circle denotes the region inside apparent horizon. Note that the density range of the color bar for APR4-29 is different from the other models.

For H4-29, ALF2-29, and PS-29, a HMNS of double-core structure is also formed while for SLy-27 a HMNS of ellipsoidal shape is formed. Irrespective of the configuration of the HMNS, however, the mass of remnant torus formed after the black hole formation is  $\simeq 0.02M_{\odot}$  and much less than that for H3-27. This suggests that the torus mass may be suppressed for a massive system, for which the total mass is close to  $M_{\text{crit}}$ ; see Eq. (15) for the definition of  $M_{\text{crit}}$ .

*Bottom* panels; H4-27 (type III). After the onset of the merger, a HMNS, which has a double-core structure, is formed as in the case of H3-27 (Fig. 1, *bottom left*). Because the lifetime of the HMNS is sufficiently long, a large amount of angular momentum is dissipated by gravitational waves. As a result, the HMNS approaches an axisymmetric ellipsoidal shape (Fig. 1, *bottom center*). After the significant loss of the angular momentum, it collapses eventually to a black hole (Fig. 1, *bottom right*). The resulting torus surrounding the formed

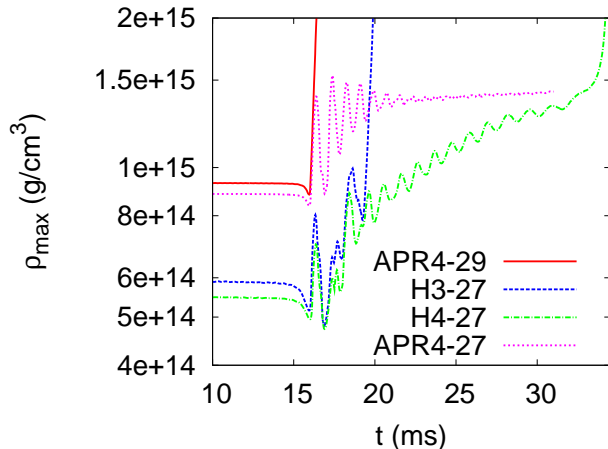


FIG. 2: The evolution of the maximum baryon rest-mass density,  $\rho_{\max}$ , for three models. The solid, dashed, dash-dotted, and dotted curves denote the results for models APR4-29 (type I), H3-27 (type II), H4-27 (type III), and APR4-27 (type III), respectively.

black hole has the maximum density  $\rho_{\max} \sim 10^{13}$  g/cm<sup>3</sup> and spreads widely to  $r \sim 25$  km. In this case, the torus mass is  $\simeq 0.18M_{\odot}$ . The resulting black hole-torus system may be regarded as a promising candidate for the central engine of short GRBs.

APR4-27, ALF2-27, and PS-27 also show the merger process of type III. For ALF2-27, the mass of the remnant torus is larger than  $0.1M_{\odot}$  as for H4-27. This suggests that with the stiff EOSs for which the maximum mass of spherical neutron stars is larger than  $2M_{\odot}$ , a massive torus could be the outcome when the total mass of the binary is  $\approx 2.7M_{\odot}$ . For PS-27 with which the maximum mass of spherical neutron stars is  $1.75M_{\odot}$ , despite type III, the mass of the remnant torus is much less ( $\simeq 0.04M_{\odot}$ ). This indicates that for the EOS with small maximum mass, the torus mass may be suppressed. More detailed reasons that could cause the difference in the remnant torus mass will be discussed in Sec. III.A.3. For APR4-27, a quasi-stationary HMNS is formed. Because the degree of differential rotation is still high and the mass is much higher than the maximum mass of spherical neutron stars, it will eventually collapse in the presence of the magnetic field or viscosity in reality (see Ref. [43]).

Figure 2 plots the evolution of the maximum baryon rest-mass density,  $\rho_{\max}$ , for models (types) APR4-29 (type I), H3-27 (type II), H4-27 (type III), and APR4-27 (type III). For APR4-29, for which a black hole is formed promptly,  $\rho_{\max}$  increases monotonically after the onset of the merger. For H3-27 and H4-27 for which a HMNS is formed transiently,  $\rho_{\max}$  oscillates and then increases until the collapse of the HMNS sets in. After the collapse of the HMNS,  $\rho_{\max}$  increases monotonically. For APR4-27,  $\rho_{\max}$  also oscillates and increases soon after the formation of the HMNS. However it eventually reaches a

relaxed value, implying that a nearly stationary HMNS is the outcome.

Figure 3 summarizes the type of the merger process for each EOS and for each mass. We find that a HMNS is likely to be formed for the merger with the EOS which provides a small compactness,  $M/R$ , for each neutron star. The reason is as follows. In the case that the compactness of each neutron star is small, two neutron stars merge at a relatively large orbital separation. As a result, the merged neutron stars have large angular momentum at the onset of the merger, which helps escaping the prompt collapse to a black hole. The long-lived HMNS is also likely to be formed for a total mass  $m_0 \gtrsim 2.7M_{\odot}$  with the EOS which has the maximum mass exceeds  $2M_{\odot}$ , such as APR4, H4, and ALF2.

Note that it is practically impossible to precisely determine the lifetime of the HMNS by the numerical simulation, because the HMNS just before the collapse is marginally stable and its dynamics depends strongly on a small perturbation and thus on the grid resolution. The lifetime also depends on the treatment of the thermal effects [35], which are determined by the value of  $\Gamma_{\text{th}}$  in our simulations. However we find that our classification of the merger process depends very weakly on the grid resolution and the value of  $\Gamma_{\text{th}}$ .

## 2. The Critical mass

We define a critical mass,  $M_{\text{crit}}$ , of binary neutron stars for each EOS as follows: If the total mass of a binary neutron star,  $m_0$ , exceeds  $M_{\text{crit}}$ , a black hole is formed promptly after the onset of the merger.

We write the value of  $M_{\text{crit}}$  in terms of  $M_{\max}$  as

$$M_{\text{crit}} = kM_{\max}, \quad (15)$$

where  $k$  is a constant which depends on the EOS. Table III shows the maximum mass, the critical mass, and their ratio,  $k$ , for each EOS together. Here we find that  $k$  is in the range,

$$1.3 \lesssim k \lesssim 1.7, \quad (16)$$

where  $k \simeq 1.3$  for APR4 ( $R_{1.4} = 11.428$  km) and SLy ( $R_{1.4} = 11.736$  km) and  $k \simeq 1.7$  for PS ( $R_{1.4} = 15.472$  km). We find the correlation between  $k$  and  $R_{1.4}$ , in which  $k$  is approximately an increasing function of  $R_{1.4}$ . Note that the results for APR4 and SLy agree with those in the previous papers [13, 14].

Recent observation suggests  $M_{\max} \geq 1.97 \pm 0.04M_{\odot}$  in one  $\sigma$  level [32]. This fact and our results suggest that a HMNS is likely to be formed transiently soon after the onset of the merger for a binary neutron star merger with the typical total mass,  $m_0 \simeq 2.7M_{\odot}$  [42].

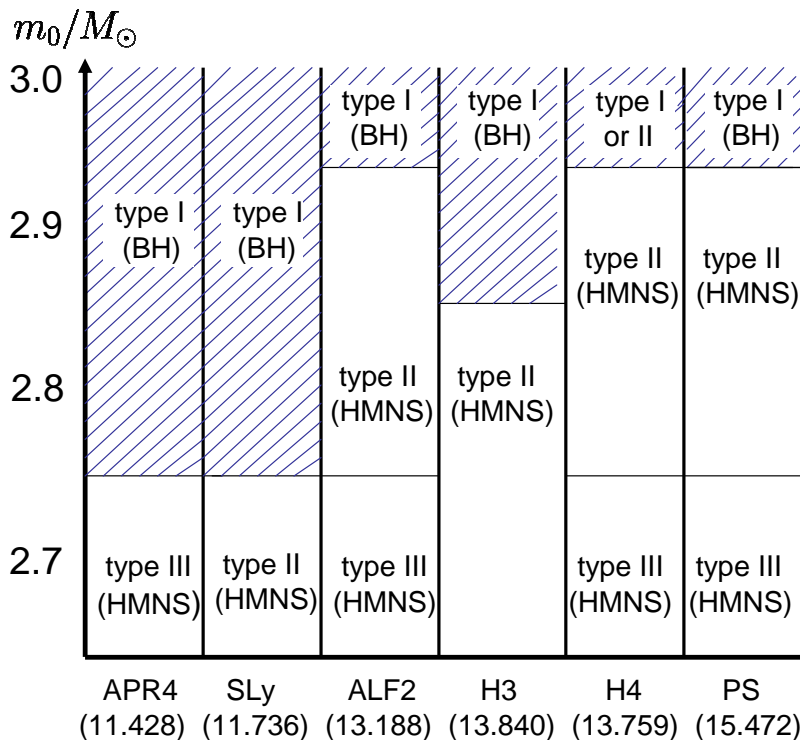


FIG. 3: Type of the merger process and the remnants for each model. The vertical axis shows the total mass of two neutron stars. The horizontal axis shows the EOSs together with their radii for  $M = 1.4M_\odot$ ,  $R_{1.4}$  km.

TABLE III: The maximum mass,  $M_{\max}$ , the critical mass,  $M_{\text{crit}}$ , and their ratio  $k$  for each EOS.

|                           | APR4         | SLy          | ALF2         | H3           | H4            | PS           |
|---------------------------|--------------|--------------|--------------|--------------|---------------|--------------|
| $k$                       | 1.3          | 1.3          | 1.4          | 1.6          | 1.5           | 1.7          |
| $M_{\max}/M_\odot$        | 2.213        | 2.049        | 2.086        | 1.788        | 2.032         | 1.755        |
| $M_{\text{crit}}/M_\odot$ | $\simeq 2.8$ | $\simeq 2.8$ | $\simeq 3.0$ | $\simeq 2.9$ | $\gtrsim 3.0$ | $\simeq 3.0$ |

### 3. Final states: Black hole and Torus

As summarized in Sec. III.A.1, after the merger of a binary neutron star, a black hole surrounded by a torus is eventually formed (see Fig. 1). Our interest here is to study how the amount of the torus mass depends on the type of the merger process. Figure 4 shows the evolution of the torus mass for models (types) APR4-29 (type I), H3-27 (type II), and H4-27 (type III). Here the time at the black hole formation is set to be  $t = 0$ . Table II shows the results for the torus mass as well as the type of the merger process for each model. We find that the torus mass is correlated to the type of the merger process as follows,

$$M_{\text{torus}} \lesssim 0.01M_\odot \quad \text{for type I,} \quad (17)$$

$$0.02M_\odot \lesssim M_{\text{torus}} \lesssim 0.05M_\odot \quad \text{for type II,} \quad (18)$$

$$0.04M_\odot \lesssim M_{\text{torus}} \lesssim 0.18M_\odot \quad \text{for type III.} \quad (19)$$

Here the torus mass is evaluated at about 1 ms after the black hole formation. Thus, the torus mass is larger in the case that a HMNS is formed than that a black hole is formed promptly. When a long-lived HMNS is formed, in particular, the resulting torus mass could be  $M_{\text{torus}} \geq 0.1M_\odot$  for many EOSs. This feature can be understood as follows. In the HMNS, its envelope spins up because angular momentum is transported from inner to outer parts of the HMNS by gravitational torques caused by the non-axisymmetric structure. As a result, a part of the matter in the envelope of the HMNS, which has sufficient angular momentum, does not fall into the black hole at the collapse of the HMNS and it constitutes the torus. However, we note that the efficiency of the angular momentum transport depends on the density profile and the degree of non-axisymmetry of the HMNS, which depend on the EOS and the total mass. For PS-27, indeed, the resulting torus mass is only  $\approx 0.04M_\odot$  which is much less than those for APR4-27, H4-27, and ALF2-27. Thus, for a special EOS which leads to a large radius

and a small maximum mass such as  $R_{1.4} \simeq 15.5$  km and  $M_{\text{max}} \simeq 1.76M_{\odot}$ , the torus mass may be small even if the merger process is type III.

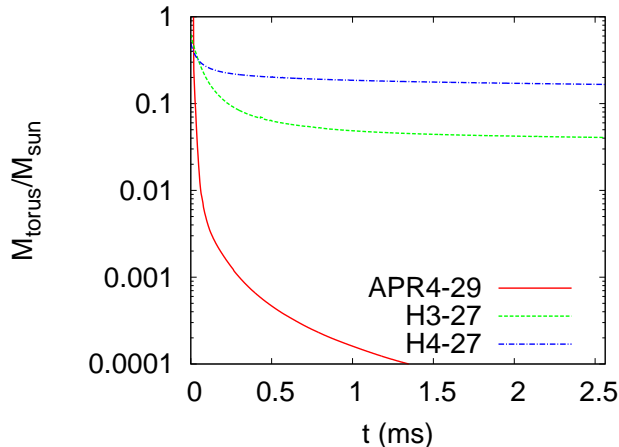


FIG. 4: The evolution of the torus mass,  $M_{\text{torus}}$ , for three models. The solid, dashed, and dash-dotted curves denote the results for models APR4-29 (type I), H3-27 (type II), and H4-27 (type III), respectively. The time at the black hole formation is set to be  $t = 0$ .

Note that, in this study, we performed numerical simulations only for the equal-mass systems. For unequal-mass systems, a massive torus may be formed even for the case that the merged neutron stars collapse promptly to a black hole. This is because the heavier star can disrupt the less massive companion by tidal forces, in particular, for high mass ratio and subsequent angular momentum transport in the spiral arms formed from the tidally disrupted neutron star enhances the torus formation, as indicated in Refs. [44–46].

## B. Gravitational Waves

Gravitational waves are emitted during the merger until a stationary black hole is formed. The gravitational waveforms reflect the dynamical behavior of the merger process. In the following, we classify the gravitational waveforms and their spectra into three types in the same way as the merger process, and discuss their features.

### 1. Gravitational waveforms

The gravitational waveforms for models APR4-27, H3-27, H4-27, and PS-27 together with post-Newtonian waveforms, calculated by the so-called Taylor T4 formula [47], are shown in Figs. 5 (1a) – (4a). For more massive models APR4-29 and H4-29 the gravitational waveforms are shown in Figs. 6 (5a) and (6a). The gravitational waveform for the inspiral phase is similar for all

the models. In the late inspiral stage, the gravitational-wave phase starts deviating from the post-Newtonian one at 3 – 5 ms before the onset of the merger. This is because the effects of the finite size of two neutron stars play an important role for their orbital motion. A detailed analysis for the finite-size effect will be published in a future paper. In the following, we focus on the gravitational waveform of the merger and the ringdown phases.

*Type I.* The gravitational waveform for APR4-29 is shown in Fig. 6 (5a). The amplitude of gravitational waves increases gradually in the inspiral phase until the merger sets in at  $t \simeq 22$  ms. Soon after the onset of the merger, ringdown gravitational waves are emitted by the oscillating black hole for  $\sim 1$  ms. Then the amplitude approaches zero because the black hole becomes stationary.

*Type II.* A short-lived HMNS is formed after the onset of the merger. Then the oscillating and rotating HMNS emits quasiperiodic gravitational waves. The gravitational waveform of H3-27 is shown in Fig. 5 (2a). In this case, two neutron stars merge at  $t \simeq 18$  ms, at which the amplitude of gravitational waves is small transiently. This implies that the merged object has a nearly axisymmetric ellipsoidal shape at the moment. After this, the core bounces and the HMNS is formed, which has a double-core structure. Then quasiperiodic gravitational waves with a high amplitude are emitted. At  $t \simeq 23$  ms, the amplitude of gravitational waves damps suddenly. This is because the HMNS collapses to a black hole before the HMNS becomes an axisymmetric ellipsoidal shape. A similar waveform is also seen for H4-29 in Fig. 6 (6b).

*Type III.* The gravitational waveform of H4-27 is shown in Fig. 5 (3a). In this case, two neutron stars merge at  $t \simeq 18$  ms, at which the amplitude of gravitational waves is small transiently as in H3-27. After this, a non-axisymmetric HMNS of the double-core structure is formed and it emits quasiperiodic gravitational waves. For  $t \gtrsim 30$  ms, gravitational waves of small amplitude is emitted quasi-stationarily until  $t \sim 37$  ms. During this phase, the HMNS has a nearly axisymmetric ellipsoidal shape. At  $t \simeq 37$  ms, the HMNS collapses to a black hole and the amplitude of gravitational waves damps eventually.

For APR4-27 (see Fig. 5 (1a)), an ellipsoidal HMNS is formed after the onset of the merger, and thus, quasiperiodic gravitational waves are emitted for the first  $\sim 10$  ms after the formation of the HMNS. The HMNS loses angular momentum due to the gravitational radiation reaction and the ellipticity gradually decreases, resulting in the decrease of the gravitational-wave amplitude. Thus, the gravitational waveform is similar to that for H4-27. However, the lifetime of the HMNS for APR4-27 is much longer than 15 ms. Thus we did not follow the collapse of the HMNS for APR4-27.

For PS-27 (see Fig. 5 (4a)), the gravitational waveform is different from those of H4-27 and APR4-27. In this case, it is similar to those for H3-27 and H4-29:

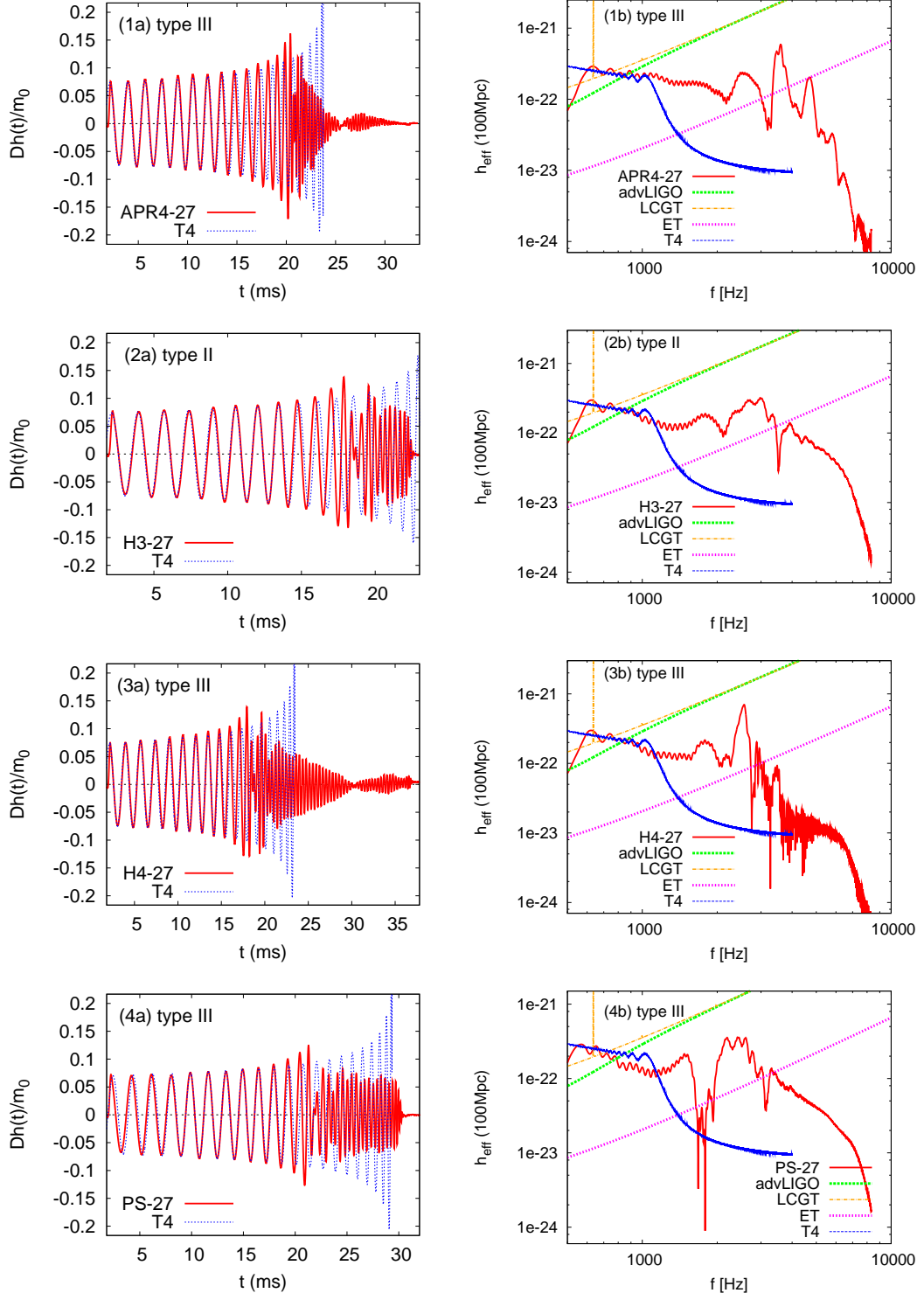


FIG. 5: Gravitational waveforms and their spectra. The solid and dashed curves in the left panels denote the waveforms calculated by the simulation and Taylor T4 formula, respectively. The solid and dashed curves in the right panels denote the spectra calculated by the simulation, and spectrum calculated by Taylor T4 formula, respectively, at a hypothetical source distance of 100 Mpc. The effective amplitude for the most optimistic direction of the source is shown. Here the noise levels of advanced LIGO (Optimal NSNS version), LCGT (Broadband version), and Einstein Telescope are shown together. (1a) and (1b) for APR4-27 (type III), (2a) and (2b) for H3-27 (type II), (3a) and (3b) for H4-27 (type III), (4a) and (4b) for PS-27 (type III).

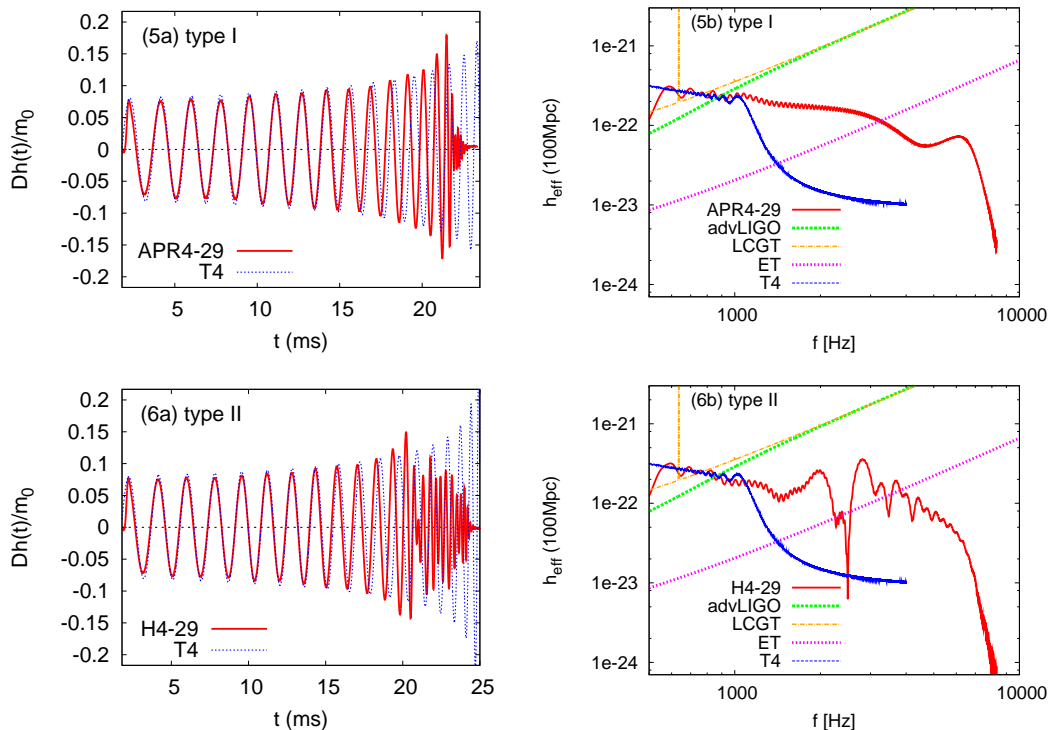


FIG. 6: The same as Fig. 5 but for  $m_0 = 2.9M_\odot$ . (5a) and (5b) for APR4-29 (type I), (6a) and (6b) for H4-29 (type II).

A HMNS of double-core structure is formed after the onset of the merger, and emits quasiperiodic gravitational waves. After a substantial emission of gravitational waves, the HMNS collapses to a black hole before it becomes a nearly axisymmetric ellipsoid.

## 2. Spectra

The right panels of Figs. 5 and 6 show the spectra of gravitational waves for models APR4-27, H3-27, H4-27, PS-27, APR4-29, and H4-29 together with the spectrum calculated by the post-Newtonian approximation (Taylor T4), and the sensitivity curves of advanced LIGO (Optimal NSNS version) [48], of LCGT (Broadband version) [7], and of Einstein telescope [49]. Here we assume that gravitational waves are observed at a distance of 100 Mpc from the sources along the most optimistic source direction. The common feature for each type is that the effective amplitude,  $h_{\text{eff}}$ , decreases with the increase of  $f$  until  $f \simeq 1$  kHz, in the inspiral phase. The spectrum shape above  $f \simeq 7$  kHz is also qualitatively the same irrespective of the model, which is caused by the quasi-normal-mode oscillations of the remnant black hole. However, the spectrum shape between 1 kHz and 7 kHz, for which gravitational waves are emitted in the merger phase, depends strongly on the EOS and on the total mass as summarized in the following:

*Type I.* Because no HMNS is formed, the shape of the spectrum is quite simple (see Fig. 6 (5b)). The effective amplitude decreases monotonically until  $f \simeq 5$  kHz. Note that the power of the spectrum shape changes at  $f \simeq 3$  kHz. This frequency is called the cut-off frequency, which is related to the compactness of two neutron stars (see Ref. [44] for details). The bump around  $f \simeq 6$  kHz is caused by the rotation of the merged object just before the collapse to a black hole (see Fig. 1, *top center*). We find that this bump is enhanced in the case that the total mass is close to the critical mass,  $m_0 \simeq M_{\text{crit}}$ .

*Type II.* A spectrum shape of type II is shown in Figs. 5 (2b) and 6 (6b). In this case, we find several peaks caused by the rotation and oscillation modes of the HMNS. There is the maximum peak at  $f \simeq 2.5$ – $3$  kHz caused by the rotation of the HMNS. The frequency of this peak is higher for the more compact HMNS, because the angular velocity of the merged neutron stars is approximately written by  $\Omega \propto m_0^{1/2}/R_{\text{ns}}^{3/2}$  at the onset of the merger. Here  $R_{\text{ns}}$  is the radius of two neutron stars. However, the peaks in the spectrum are too small to be detected by the advanced detectors such as advanced LIGO and LCGT for  $D = 100$  Mpc, because the lifetime of the HMNS is short and the accumulated gravitational-waves cycles are small. There is a shallow decay of the spectrum around  $4 \lesssim f \lesssim 7$  kHz. This is the common feature in the case that a HMNS is formed (see Figs. 5 (2b)–(4b), and 6 (6b)).

*Type III.* Figures 5 (1b) and 5 (3b) show the spectrum shape of APR4-27 and H4-27. We find that the peak amplitude of the spectrum at  $f \simeq 2.5$  kHz is larger than that for type II and the primary oscillation mode appears clearly. Note that the amplitude of the peak is slightly smaller than the sensitivity curve of advanced LIGO (Optimal NSNS version) and LCGT (Broadband version) for a hypothetical distance of 100 Mpc. If this peak could be observed with optimized detectors or for an event of short distance, we would get information about the physics of HMNSs and could constrain the supernuclear-density EOS [50].

Note that the spectrum shape for type III depends on the EOS. For example, the spectrum shape of PS-27 is different from that for APR4-27 and H4-27 (see Fig. 5 (1b), 5 (3b), and Fig. 5 (4b)). The bump around the maximum peak at  $f \simeq 2.5$  kHz in the spectrum of PS-27 is broader than that of H4-27.

#### IV. SUMMARY AND DISCUSSION

We studied the dependence of the dynamical behavior of the binary neutron star merger on the EOS of the supernuclear-density matter in numerical relativity with piecewise-polytropic EOSs. We performed numerical simulations for 6 stiff EOSs and for several total masses in the range of  $2.7M_{\odot}$ – $3.0M_{\odot}$ . For all the cases, the equal-mass binary system was considered.

We classified the merger process into three types: (i) a black hole is promptly formed (type I); (ii) a short-lived HMNS is formed (type II); (iii) a long-lived HMNS is formed (type III). For a given total mass of the binary neutron star, the type of the merger process depends strongly on the EOS. In particular, the compactness of the neutron stars and the maximum mass of spherical neutron stars for a given EOS are key quantities for determining whether a HMNS is formed transiently or not. We found that the critical mass of the prompt formation of a black hole is in the range of  $1.3 \lesssim M_{\text{crit}}/M_{\text{max}} \lesssim 1.7$ . The latest observation of the high-mass neutron star with mass  $1.97 \pm 0.04M_{\odot}$  suggests that  $M_{\text{crit}}$  is larger than  $2.7M_{\odot}$ . These facts indicate that a HMNS should be formed at least transiently for the total mass of the binary neutron stars,  $m_0 \sim 2.6M_{\odot}$  or less. We found that a long-lived HMNS is formed for  $m_0 \sim 2.7M_{\odot}$  and for the EOS with which the maximum mass of spherical neutron stars exceeds  $2M_{\odot}$ , such as APR4 and H4.

We studied the properties of a torus around a black hole formed after the merger. We found that the torus mass depends strongly on the type of the merger process. Specifically, the range of the torus mass is  $M_{\text{torus}} \lesssim 0.01M_{\odot}$  for type I,  $0.02M_{\odot} \lesssim M_{\text{torus}} \lesssim 0.05M_{\odot}$  for type II, and  $0.04 \lesssim M_{\text{torus}} \lesssim 0.18M_{\odot}$  for type III. Thus we found that the torus mass is larger in the case that the HMNS is formed than in the case that a black hole is formed promptly. This is because materials in the outer

envelope of the HMNS receive angular momentum from the central part via gravitational torques which work on the non-axisymmetric ellipsoidal HMNS. As a result, a part of the materials in the outer envelope does not fall into the black hole soon after the collapse of the HMNS and remains around the black hole to be a torus. In this sense, we conclude that the HMNS will play an important role for the merger scenario of short GRBs. Note that we performed numerical simulations only for the equal-mass system. For the unequal-mass case, the dynamical evolution of the merger could be modified. The heavier star may tidally disrupt the less massive companion if the mass ratio is high. As a result, the torus mass around the black hole may be enhanced (see Refs. [44–46]).

We also studied gravitational waves from the binary neutron star merger. The gravitational waveforms and their spectra depend strongly on the merger process. For type II and type III, we found that a large amount of gravitational waves are emitted by the HMNS which has a non-axisymmetric configuration. With decreasing its angular momentum, the HMNS approaches an axisymmetric ellipsoid and the amplitude of gravitational waves decreases.

The amplitude of the spectrum for type I decreases monotonically with increasing  $f$  until 3–4 kHz because the HMNS is not formed. Note that there is a bump at  $f \sim 5$ –6 kHz caused by gravitational waves emitted by a merged object just before the collapse. By contrast, for type II and type III, the spectra have a complicated shape caused by the oscillation and rotation of the HMNS. At  $f \sim 2$ –3 kHz, there is the maximum peak caused by the fundamental rotation mode of the non-axisymmetric HMNS. We also found that several peaks due to the oscillation mode coupling with the rotation exist at both sides of the maximum peak.

The detectability of gravitational waves from the HMNS is estimated. With advanced detectors such as advanced LIGO and LCGT, we may be able to detect gravitational waves caused by the rotation mode of the very long-lived HMNS ( $\tau_H \geq 10$  ms) at around  $f \sim 2$ –3 kHz if the distance to the source is much smaller than 100 Mpc. If these waves are observed, we will get information about the physics of HMNSs and may be able to constrain properties of the supernuclear-density matter [50].

#### Acknowledgments

We thank Y. Sekiguchi, Y. Suwa, and T. Nakamura for useful discussions and comments. This work was supported by Grant-in-Aid for Scientific Research (21340051), by Grant-in-Aid for Scientific Research on Innovative Area (20105004), by the Grant-in-Aid of JSPS, by HPCI Strategic Program of Japanese MEXT, and by Grant-in-Aid for Young Scientists (B) 22740178.

- 
- [1] B. P. Abbott *et al.*, Rep. Prog. Phys. **72**, 076901 (2009).
- [2] T. Accadia *et al.*, Class. Quantum Grav. **28**, 025005 (2011).
- [3] S. Hild, Class. Quantum Grav. **23**, S643 (2006).
- [4] R. O’Shaughnessy, V. Kalogera, and K. Belczynski, Astrophys. J. **716**, 615 (2010).
- [5] Advanced LIGO, <http://www.advancedligo.mit.edu/>
- [6] Advanced VIRGO, <http://www.cascina.virgo.infn.it/advirgo/>
- [7] K. Kuroda *et al.*, Class. Quantum Grav. **27**, 084004 (2010).
- [8] R. Narayan, B. Paczynski, and T. Piran, Astrophys. J. **395**, L83 (1992).
- [9] B. Zhang and P. Meazaros, Int. J. Mod. Phys. A **19**, 2385 (2004).
- [10] T. Piran, Rev. Mod. Phys. **76**, 1143 (2005).
- [11] S. Setiawan, M. Ruffert, and H.-Th. Janka, Mon. Not. R. Astron. Soc. **325**, 753 (2004); W. H. Lee, E. Ramirez-Ruiz, and D. Page, Astrophys. J. **632**, 421 (2005); M. Shibata, Y. Sekiguchi, and R. Takahashi, Prog. Theor. Phys. **118**, 257 (2007).
- [12] M. Shibata, K. Taniguchi, and K. Uryu, Phys. Rev. D **68**, 084020 (2003).
- [13] M. Shibata, K. Taniguchi, and K. Uryu, Phys. Rev. D **71**, 084021 (2005).
- [14] M. Shibata and K. Taniguchi, Phys. Rev. D **73**, 064027 (2006).
- [15] L. Biotti, B. Giacomazzo, and L. Rezzolla, Phys. Rev. D **78**, 084033 (2008).
- [16] K. Kiuchi, Y. Sekiguchi, M. Shibata, and K. Taniguchi, Phys. Rev. D **80**, 064037 (2009).
- [17] R. Oechslin, H.-Th. Janka, and A. Marek, Astron. Astrophys. **467**, 395 (2007).
- [18] J. S. Read, B. D. Lackey, B. J. Owen, and J. L. Friedman, Phys. Rev. D **79**, 124032 (2009).
- [19] F. Özel and D. Psaltis, Phys. Rev. D **80**, 103003 (2009).
- [20] T. Yamamoto, M. Shibata, and K. Taniguchi, Phys. Rev. D **78**, 064054 (2008).
- [21] M. Shibata and T. Nakamura, Phys. Rev. D **52**, 5428 (1995).
- [22] T. W. Baumgarte and S. L. Shapiro, Phys. Rev. D **59**, 024007 (1998).
- [23] M. Campanelli, C. O. Lousto, P. Marronetti, and Y. Zlochower, Phys. Rev. Lett. **96**, 111101 (2006); J. G. Barker, J. Centrella, D.-I. Choi, M. Koppitz, and J. van Meter, Phys. Rev. Lett. **96**, 111102 (2006); L. Baiotti, M. Shibata, and T. Yamamoto Phys. Rev. D **82**, 064015 (2010).
- [24] B. Brügmann, J. A. Gonzalez, M. Hannam, S. Husa, U. Sperhake, and W. Tichy, Phys. Rev. D **77**, 024027 (2008).
- [25] A. Kurganov and E. Tadmor, J. Comput. Phys. **160**, 241 (2000).
- [26] A. Akmal, V. R. Pandharipande, and D. G. Ravenhall, Phys. Rev. C **58**, 1804 (1998).
- [27] F. Douchin and P. Haensel, Astron. Astrophys. **380**, 151 (2001).
- [28] B. D. Lackey, M. Nayyar, and B. J. Owen, Phys. Rev. D **73**, 024021 (2006).
- [29] N. K. Glendenning and S. A. Moszkowski, Phys. Rev. Lett. **67**, 2414 (1991).
- [30] M. Alford, M. Brady, M. Paris and S. Reddy, Astrophys. J. **629**, 969 (2005).
- [31] V. R. Pandharipande and R. A. Smith, Nucl. Phys. **A237**, 506 (1975).
- [32] P. B. Demorest, T. Pennucci, S. M. Ransom, M. S. E. Roberts, and J. W. T. Hessels, Nature **467**, 1081 (2010).
- [33] J. M. Lattimer and M. Prakash, arXiv:1012.3208 (2010).
- [34] F. Özel, D. Psaltis, A. Ransom, P. Demorest, and M. Alford, Astrophys. J. **724**, L199 (2010).
- [35] A. Bauswein, H.-Th. Janka, and R. Oechslin, Phys. Rev. D **82**, 084043 (2010).
- [36] Y. Sekiguchi, K. Kiuchi, K. Kyutoku, and M. Shibata, submitted to Phys. Rev. Lett. (2011).
- [37] K. Taniguchi and M. Shibata, Astrophys. J. Suppl. **188**, 187 (2010).
- [38] E. Gourgoulhon, P. Grandclément, K. Taniguchi, J.-A. Marck, and S. Bonazzola, Phys. Rev. D **63**, 064029 (2001).
- [39] L. Bildsten, and C. Cutler, Astrophys. J. **400**, 175 (1992).
- [40] C. S. Kochanek, Astrophys. J. **398**, 234 (1992).
- [41] LORENE webpage: <http://www.lorene.obspm.fr/>
- [42] C. M. Zhang, J. Wang, Y. H. Zhao, H. X. Yin, L. M. Song, D. P. Menezes, D. T. Wickramasinghe, L. Ferrario, and P. Chardonnet, Astron. Astrophys. **527**, A83 (2011).
- [43] T. W. Baumgarte, S. L. Shapiro, and M. Shibata, Astrophys. J. **528**, L28 (2000).
- [44] K. Kiuchi, Y. Sekiguchi, M. Shibata, and K. Taniguchi, Phys. Rev. Lett. **104**, 141101 (2010).
- [45] M. Shibata, K. Taniguchi, and K. Uryu, Phys. Rev. D **68**, 084020 (2003).
- [46] L. Rezzolla, L. Baiotti, B. Giacomazzo, D. Link, and J. A. Font, Class. Quantum Grav. **27**, 114105 (2010).
- [47] M. Boyle, D. A. Brown, L. E. Kidder, A. H. Mroue, H. P. Pfeiffer, M. A. Scheel, G. B. Cook, and S. A. Teukolsky, Phys. Rev. D **76**, 124038 (2007).
- [48] For planned sensitivity curves for advanced LIGO, see <https://dcc.ligo.org/cgi-bin/DocDB/ShowDocument?docid=2974>
- [49] M. Punturo *et al.* Class. Quantum Grav. **27**, 194002 (2010).
- [50] M. Shibata, Phys. Rev. Lett. **94**, 201101 (2005).